Large-Scale Viscous Simulation of Laminar Vortex Flow Over a Delta Wing

Arthur Rizzi,*
Aeronautical Research Institute of Sweden, Bromma, Sweden,
Royal Institute of Technology, Stockholm, Sweden
and
Bernhard Müller†
Aeronautical Research Institute of Sweden, Bromma, Sweden

A numerical method is developed to solve the Navier-Stokes equations for laminar compressible flow around delta wings. A large-scale solution on a mesh of 129 × 49 × 65 points for transonic flow $M_\infty = 0.85$, $\alpha = 10$ deg, and $Re_{\infty,C_R} = 2.38 \times 10^6$ around a 65 deg swept delta wing with round leading edge is presented and discussed. The results reveal the presence of primary, secondary, and even tertiary vortices. Comparison with experiment shows that the interaction between the primary and secondary vortices is obtained correctly and that these results are a more realistic simulation than the one given by the Euler equations.

Introduction

NUMERICAL solution to the Euler equations currently is being proposed as a model to the problem of leading-edge separation from a delta wing and the consequent formation of a vortex over the wing. The approach seems reasonable enough and, indeed, convincing results have been produced when the separation occurs from a sharp edge.[1-3] One concern with a solution to finite differences taken on a grid is that the vorticity diffuses because of the numerical method. A mesh with a large number of grid points usually is needed in order to limit the diffusion to a low level. But even then serious reservations arise with this approach if the edge is round because the action of viscosity in the boundary layer now determines precisely where the flow separates and not a geometrical singularity as in the case of a sharp leading edge.

The comparison of Euler solutions with experimental measurements in an internationally sponsored study of vortex flow over cropped 65 deg delta wings with sharp and round leading edges recently demonstrated this point.[4] With the round leading edge a vortex is shed in some numerical Euler solutions, but in other solutions the flow is attached around the leading edge. This suggests that the Euler solution may be nonunique. Even when the numerical solution produces a vortex as expected, the comparison with the measured surface pressure is not particularly good because the secondary vortex, observed in the experiment but not in the Euler solution, displaces the position of the primary vortex. One concludes that a viscous model is needed for a more realistic simulation.

We have recently developed a numerical method to solve the compressible Navier-Stokes equations for laminar flow over delta wings.[5] We present here some of our latest results from a large-scale Navier-Stokes simulation of transonic flow $M_\infty = 0.85$ $\alpha = 10$ deg over the round-edge delta wing of the International Vortex Flow Experiment and compare them with our Euler solution and the measured pressure distributions. The viscous solution contains the secondary vortex as well as other vortices located between the upper surface of the wing and the shear layer shed from its leading edge. The comparison with the experiment shows that the position of the primary vortex and the surface pressure under its core are more accurate in the Navier-Stokes solution than in the Euler solution. Hence, the proper interaction between the primary and secondary vortices is obtained.

Received Aug. 26, 1987; revision received April 10, 1988.

*Research Scientist and Adjunct Professor. Member AIAA.

†Research Scientist; currently with German Aerospace Research Establishment (DFVLR), Institute for Theoretical Fluid Mechanics, Göttingen, FRG.

Computational Method

The Navier-Stokes equations for an arbitrary stationary cell V with boundary ∂V and outer normal unit vector $\boldsymbol{n}$ in a Cartesian reference frame read

$$\int_V \frac{\partial \boldsymbol{q}}{\partial t}\,dV + \int_{\partial V} \underline{H}(\boldsymbol{q})\cdot \boldsymbol{n}\,dA = 0 \tag{1}$$

where

$$\boldsymbol{q} = \begin{bmatrix} \rho \\ \rho \boldsymbol{v} \\ e \end{bmatrix} \qquad \underline{H} = \begin{bmatrix} \rho \boldsymbol{v} \\ \rho \boldsymbol{v}\boldsymbol{v} + p\underline{I} - \underline{\tau} \\ (e+p)\boldsymbol{v} - \underline{\tau}\cdot\boldsymbol{v} + \boldsymbol{Q} \end{bmatrix}$$

The notation is standard. The column vector $\boldsymbol{q}$ is density, momentum, and total energy per unit volume. The gas is air and is considered perfect. Newton's law gives the stress tensor

$$\underline{\tau} = \mu[\text{grad } \boldsymbol{v} + (\text{grad } \boldsymbol{v})^T] + \lambda \underline{I} \text{div } \boldsymbol{v}$$

and Fourier's law the heat flux $\boldsymbol{Q}$. The viscosity coefficient μ depends on temperature according to Sutherland's law, and the Prandtl number is assumed constant, $Pr = 0.72$.

Spatial Discretization

The Navier-Stokes equations [Eq. (1)] are discretized in hexahedrons (Fig. 1) using the finite-volume technique. Since the conservative variables are assumed to be defined by their cell averages, the volume integral in Eq. (1) over a cell P is expressed by:

$$\int_{V_P} \frac{\partial \boldsymbol{q}}{\partial t}\,dV = \frac{\partial \boldsymbol{q}_P}{\partial t}\int_{V_P} dV \tag{2}$$

The surface integral in Eq. (1) over the boundary of cell P is approximated by assuming the mean-value of the flux tensor

on each side to be equal to the arithmetic average of the flux tensor in the adjacent cells:

$$\int_{\partial V_P} \underline{H} \cdot \boldsymbol{n}\, \mathrm{d}A \cong \sum_{k=1}^{6} \underline{H}_{Pk} \cdot \int_{\partial V_{Pk}} \boldsymbol{n}\, \mathrm{d}A \tag{3}$$

where

$$\underline{H}_{Pk} = \tfrac{1}{2}\,(\underline{H}_P + \underline{H}_k)$$

and ∂V_{Pk} denotes the common part of the boundaries of P and its neighboring cell k.

With the conservative variables given, all terms of the flux tensor are readily available in cell P, except for the gradients of the velocity components and temperature as well as div v. Following the definition of the conservative variables as cell averages,[5] the gradients in cell P are defined by:

$$\text{grad}\ \phi_P = \int_{V_P} \text{grad}\ \phi\ \mathrm{d}V \Big/ \int_{V_P} \mathrm{d}V \tag{4}$$

where $\phi = u, v, w,$ or T.

Using the gradient theorem, the volume integral in Eq. (4) can be expressed by a surface integral, which is approximated similarly to Eq. (3):

$$\text{grad}\ \phi_P = \int_{\partial V_P} \phi\, \boldsymbol{n}\, \mathrm{d}A \Big/ \int_{V_P} \mathrm{d}V \cong \sum_{k=1}^{6} \phi_{Pk} \int_{\partial V_{Pk}} \boldsymbol{n}\, \mathrm{d}A \Big/ \int_{V_P} \mathrm{d}V \tag{5}$$

where

$$\phi_{Pk} = \tfrac{1}{2}\,(\phi_P + \phi_k)$$

div v_p is evaluated similarly to grad ϕ_P.

On a Cartesian equidistant grid, the present finite-volume approximation is equivalent to a second-order central difference discretization involving 25 points. It is broader than the conventional finite-volume scheme applied to the Navier-Stokes equations that involve 19 points.

Numerical Damping

The spatial discretization constitutes the physical difference operator $\boldsymbol{F}_{PH}$ defined by the negative right-hand side of Eq. (3) divided by the cell volume. The convective central differences do not damp unphysical oscillations caused by flow discontinuities and waves with short wavelengths, nor do the dissipative central differences because our broad scheme uncouples neighboring points. Therefore, we add numerical damping terms $\boldsymbol{F}_N(q)$ just as we did for solving the Euler equations,[6] but we use smaller coefficients. They comprise non-linear, second-order differences sensed by the discretized second derivative of the pressure, and linear fourth-order differences of the conservative variables:

$$\boldsymbol{F}_N(q) = (CFL/\Delta t)\{\chi(\delta_I[s_I(p)\delta_I] + \delta_J[s_J(p)\delta_J] + \delta_K[s_K(p)\delta_K]) - \Lambda(\delta_I^4 + \delta_J^4 + \delta_K^4)\}q \tag{6}$$

with CFL the maximum CFL number used (defined below) and Δt the time step. The constants χ and Λ used lie in the ranges: $0 \le \chi \le 0.01$ and $0.005 \le \Lambda \le 0.02$. The sensors s_I, s_J and s_K are of similar form, e.g., s_I for a cell indexed by I,J,K:

$$s_I(p_{I\pm\frac{1}{2},J,K}) = \mu_I\, |\delta_I^2\, p_{I\pm\frac{1}{2},J,K}| \Big/ \max_{I',J',K'} |\delta_I^2\, p_{I',J',K'}| \tag{7}$$

Here the classical finite-difference operators are defined by:

$$\delta_I\, \phi_{I,J,K} = \phi_{I+\frac{1}{2},J,K} - \phi_{I-\frac{1}{2},J,K}$$

$$\mu_I\, \phi_{I,J,K} = (\phi_{I+\frac{1}{2},J,K} + \phi_{I-\frac{1}{2},J,K})/2 \tag{8}$$

and similarly for J and K.

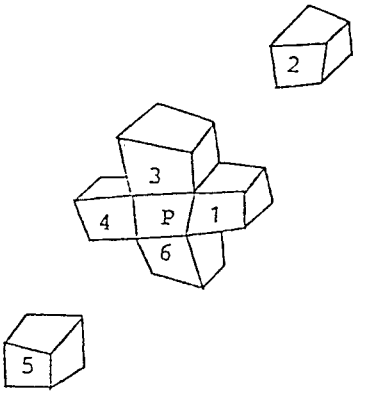

Fig. 1 Basic hexahedron P and neighboring cells 1 to 6 (2 and 5 set apart).

The numerical damping operator $\boldsymbol{F}_N$ is modified near the wing surface and farfield to ensure its dissipative property also there.

Time Integration

Thus, the semidiscrete approximation of the Navier-Stokes equations can be written as:

$$\frac{\mathrm{d}q}{\mathrm{d}t} = \boldsymbol{F}(q) \tag{9}$$

where

$$\boldsymbol{F} = \boldsymbol{F}_{PH} + \boldsymbol{F}_N$$

Equation (9) represents a large system of first-order ordinary differential equations. We solve it for the steady state by the second-order explicit three-stage Runge-Kutta scheme:

$$\begin{aligned} q^0 &= q^n \\ q' &= q^0 + \Delta t\, \boldsymbol{F}(q^0) \\ q'' &= q^0 + \tfrac{1}{2}\Delta t[\boldsymbol{F}(q^0) + \boldsymbol{F}(q')] \\ q^{n+1} &= q^0 + \tfrac{1}{2}\Delta t[\boldsymbol{F}(q^0) + \boldsymbol{F}(q'')] \end{aligned} \tag{10}$$

Stability

The stability of explicit Runge-Kutta schemes applied to the semidiscretization [Eq. (9)] of the Navier-Stokes equations has been studied for a scalar linear model equation in Ref. 5. If the coefficients of the model equation are obtained from the maximum moduli of the eigenvalues of the coefficient matrices of the linearized Navier-Stokes equation, the von Neumann stability analysis shows that also the mixed derivatives contribute to the time step limitation even on an orthogonal mesh, contrary to the implication we reached in Ref. 5. We have refined the stability condition for an explicit Runge-Kutta method applied to the present finite-volume discretization of the Navier-Stokes equations. The estimate we now use reads

$$\begin{aligned} \Delta t \le \min\ \{ & CFL\ vol[|v \cdot S_I| + |v \cdot S_J| + |v \cdot S_K| \\ & + c(|S_I| + |S_J| + |S_K|)]^{-1}, \\ & \tfrac{1}{2}|RK|\, vol^2[\nu(|S_I|^2 + |S_J|^2 + |S_K|^2) \\ & + 2\nu(|S_I \cdot S_J| + |S_I \cdot S_K| + |S_J \cdot S_K|) \\ & + ((\lambda + \mu)/\rho)(|S_I|\,|S_J| + |S_I|\,|S_K| + |S_J|\,|S_K|)]^{-1}\} \end{aligned} \tag{11}$$

where c is the speed of sound, $\nu = \max(\mu, \lambda + 2\mu, \gamma\mu/Pr)/\rho$, vol the cell volume, S_I the surface normal in I-direction, etc.

The stability bounds RK and CFL are chosen such that all complex numbers z with $RK \le \mathrm{Re}(z) \le 0$ and $|\mathrm{Im}(z)| \le CFL$ lie inside the stability region of the Runge-Kutta method (see Fig. 2). For the three-stage Runge-Kutta method [Eq. (10)] the following choice is taken for the delta wing fine-mesh case: $CFL = 0.5$ and $RK = -1$. In general, $CFL = 1.5$ and $RK = -1$ are taken. The factor ½ leaves space on the negative real axis of the stability region to accommodate the numerical damping contribution.

Mesh

The round leading-edge delta wing proposed for the International Vortex Flow Experiment on Euler Code Validation has 65 deg sweep and 15% taper. It is defined by one section in terms of x and z coordinates:

$$z = \begin{cases} \pm [0.1183\sqrt{x} - 0.2101x + 0.3501x^2 - 0.3406x^3 & \\ & 0 \le x \le 0.4 \\ \text{NACA 64A005 profile} & x > 0.4 \end{cases}$$

The nose radius is 0.7%, the maximum thickness is 5% of the local chord at $x = 0.4$, and the trailing edge is sharp.

We generate an O-O mesh around this wing by the transfinite interpolation method.[7] The fine mesh consists of 129, 49, and 65 grid points in the chordwise I, near normal J, and spanwise K directions, respectively, i.e., 410,865 grid points in total. On the wing the mesh points are clustered near the leading edge and tip and to a lesser extent also near the trailing edge and symmetry boundary with larger spacings in the midsections (Fig. 3). The mesh is nearly orthogonal at the wing contour, except for the points near the trailing edge and tip (Figs. 4 and 5). The grid points between the wing and the far field, which is a hemisphere of radius 3 root chords C_R from midroot-chord, are clustered near the wing to resolve the boundary layer. We estimate that the clustering places about 20 points in the boundary layer.

Initial and Boundary Conditions

For $M_\infty = 0.85$, $\alpha = 10$ deg, $Re_{\infty,C_R} = 2.38 \times 10^6$, the calculation is started from freestream on a coarse mesh using a large second-order damping coefficient ($\chi = 0.1$), which is subsequently reduced to 0.01. The converged result is interpolated on the medium mesh and so on to the fine mesh.

The O-O mesh topology introduces periodic, symmetry, wing, and far-field boundaries to determine bilaterally symmetric flow over a quadrilateral wing. The symmetry boundary lies in the $y = 0$ plane. The periodic boundaries extend from the trailing edge and tip of the wing in the positive x and y directions, respectively. At periodic boundaries, grid points on upper and lower surfaces are mapped onto each other. The conditions on the conservative variables are

$$q_{I\mathrm{MAX},J,K} = q_{1,J,K}, \quad q_{I,J,K\mathrm{MAX}} = q_{I\mathrm{MAX}-I,J,K\mathrm{MAX}-1} \tag{12a}$$

At the symmetry boundary, ρ, u, w, and e are even functions with respect to y, and v is an odd one:

$$(\rho,u,v,w,e)^T(x,y,z) = (\rho,u,-v,w,e)^T(x,-y,z) \tag{12b}$$

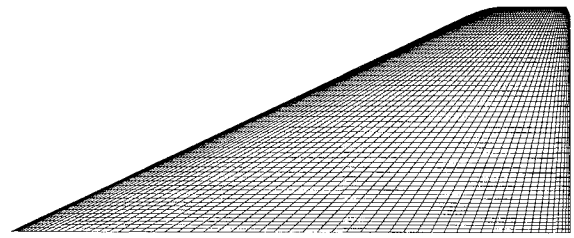

Fig. 3 Surface mesh of 65 deg swept cropped delta wing.

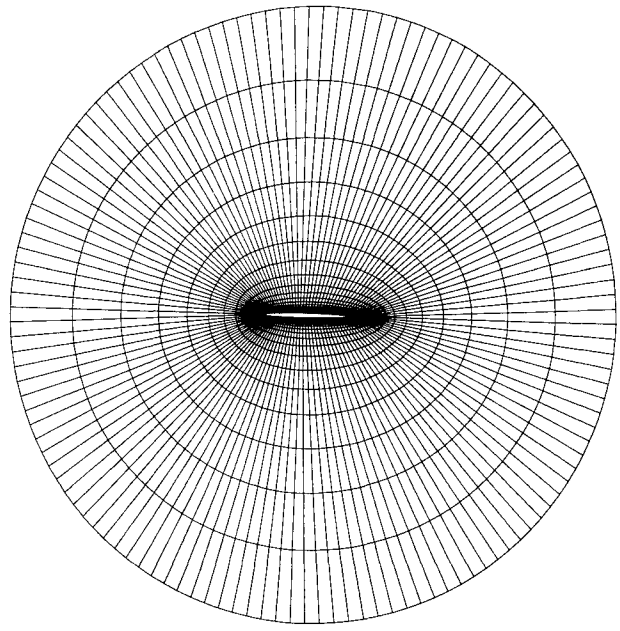

a) Global view

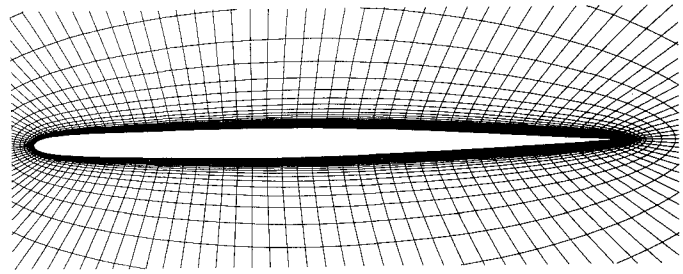

b) Enlargement

Fig. 4 Mesh in plane of symmetry.

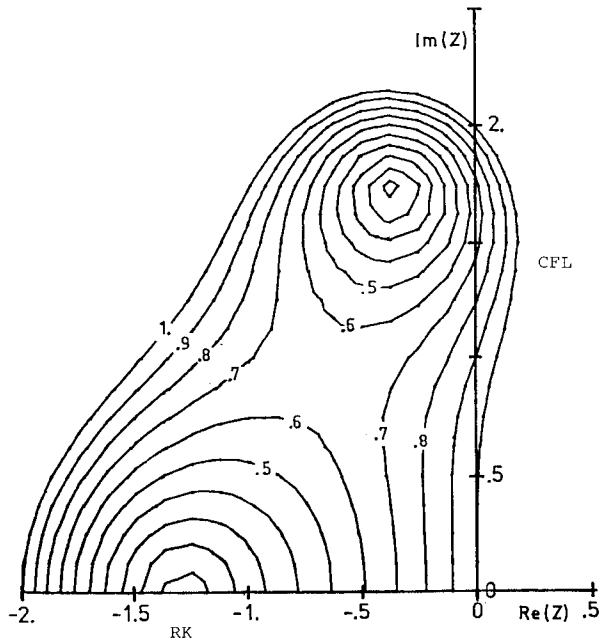

Fig. 2 Contours of constant modulus of growth factors of scheme (10) and stability bounds RK and CFL.

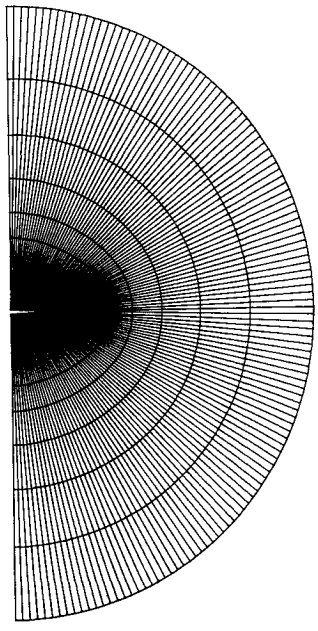

a) Global view

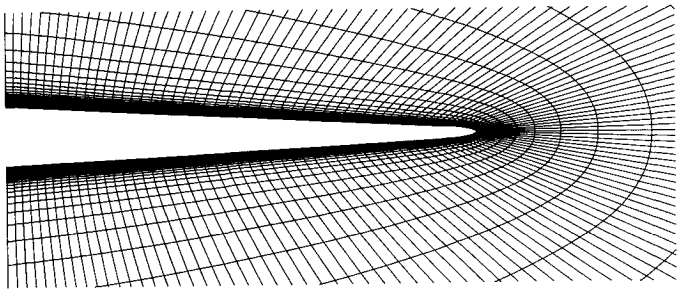

b) Enlargement

Fig. 5 Mesh in surfaces I = 33 and 97 seen from behind (at ~37% local chord on wing).

The no-slip condition holds on the wing, which is assumed to be adiabatic. The pressure is obtained by neglecting the viscous terms in the wall normal momentum equation:

$$v_w = 0, \quad \left.\frac{\partial T}{\partial n}\right|_w = 0, \quad \left.\frac{\partial p}{\partial n}\right|_w = 0 \tag{12c}$$

The pressure and the stress tensor at the wing interface of the first cell above the wing are approximated by their values in that cell.

The boundary conditions at the far-field boundary are based on the theory of characteristics for locally one-dimensional inviscid flow. For supersonic inflow or outflow, the locally one-dimensional Riemann invariants, entropy and tangential velocity component, i.e.:

$$R_1 = \boldsymbol{v}\cdot\boldsymbol{n} - \frac{2}{\gamma-1}c, \qquad R_2 = \boldsymbol{v}\cdot\boldsymbol{n} + \frac{2}{\gamma-1}c$$

$$R_3 = \ell n\left(\frac{p}{\rho^\gamma}\right), \qquad R_4 = \boldsymbol{v} - (\boldsymbol{v}\cdot\boldsymbol{n})\boldsymbol{n} \tag{12d}$$

are given from outside or inside the computational region by, respectively:

$$R_m = R_{m_\infty} \quad \text{or} \quad \frac{\partial R_m}{\partial n} = 0 \tag{12e}$$

For subsonic inflow, R_1, R_3, and R_4 are given from outside and R_2 from inside; R_2, R_3, and R_4 are determined from inside and R_1 from outside for subsonic outflow.

The conditions [Eq. (12e)] are used to determine R_m in a fictitious cell outside the domain of integration either by freestream or by R_m in the cell next to the farfield.

This fully discrete explicit scheme has been fully vectorized over all three dimensions for the CYBER 205 supercomputer by the vector-coding concept developed by Rizzi.[8] Using 32-bit word length, the resulting computer program operates at 23 CPU microseconds per time step and per grid point. Only 30 data quantities need to be stored at each grid point.

Discussion of Computed Solution

We simulate laminar flow over the cropped delta wing for the conditions $M_\infty = 0.85$, $\alpha = 10$ deg, and $Re_{\infty,c_R} = 2.38 \times 10^6$. The streamlines (steady particle paths) originating near the leading edge in Fig. 6 show two distinct regions of swirling flow that lift before the trailing edge. The inboard one is clearly the primary vortex and is above the outboard region. The other swirling that we see only starts past midchord. For this reason and because it is too far outboard, we hesitate to call it the secondary vortex. We discuss this further below. The side view shows that the shear layer leaving from the cropped tip is less tightly wound, presumably because of the reduced sweep angle of this edge. We remark that there is no indication of an abrupt uplifting of the vortex near the beginning of the cropped tip, as we have seen in the corresponding Euler solution.[13] We attributed that as an effect of the cropped edge.

The line toward which the skin friction lines converge (Fig. 7) clearly indicates the secondary separation at $y/s \approx 0.74$ and confirms that there is a secondary vortex in the numerical solution. This compares reasonably well with the oil flow in Fig. 7, considering that the experiment is done for a wing with a sharp leading edge. The experiment indicates a clear primary attachment line, and one can infer one in the computations up to about 60% chord. Past this point the skin friction lines from near the symmetry plane are swept spanwise outboard, and the suggestion of a primary attachment line is completely lost. Since this is just ahead of the cropped tip, perhaps this effect is linked to the tip. But the discrepancy that we cannot explain is that close to the trailing edge the computed lines sweep outboard from the symmetry plane, while the oil flow shows the direction to be streamwise inboard of the primary attachment. The skin friction lines emanating from points a short distance away from the tip and trailing edge turn upstream and apparently terminate in a nodal point of separation on the secondary separation line, also in contrast to the oil flow.

Figure 8 presents the computed skin friction lines on the upper side of the leading edge. Where they are converging, the dashed line nearest the leading edge has been drawn to indicate

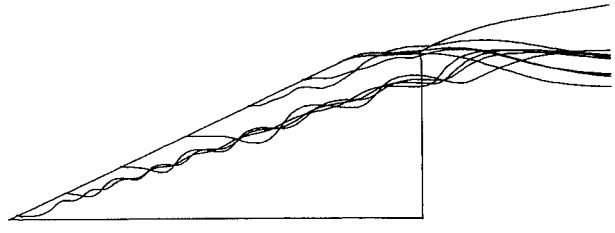

a) View from above

b) Horizontal view toward symmetry plane

Fig. 6 Streamlines originating near the leading edge determined from the solution show multiple vortices over the wing.

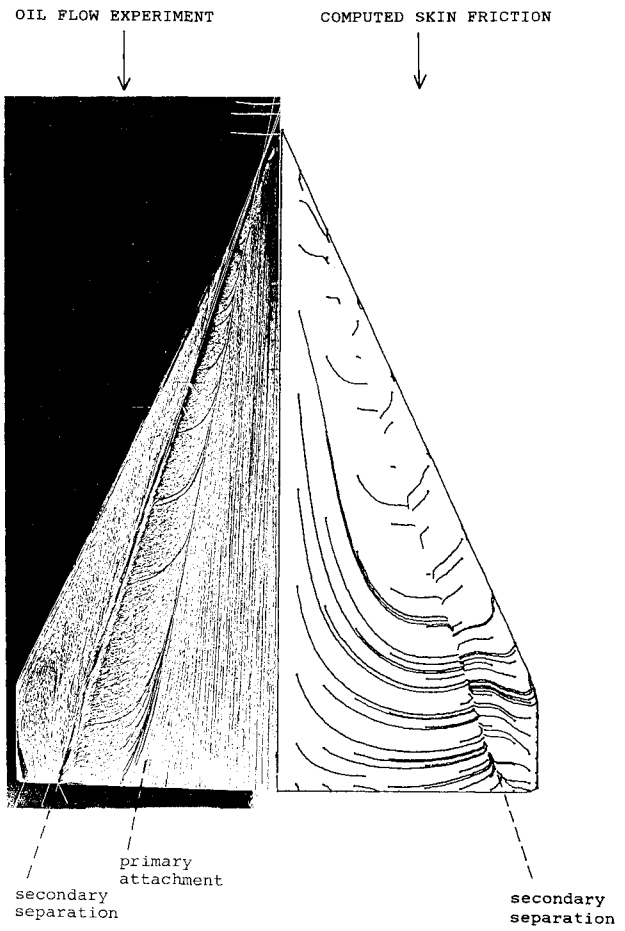

Fig. 7 Comparison of oil flow photograph[9] with skin friction lines computed in the Navier-Stokes solution.

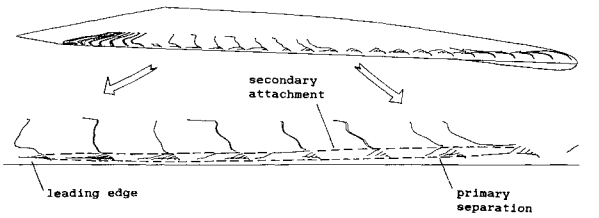

Fig. 8 Skin friction lines on the leading edge indicate the primary separation line and the secondary attachment line.

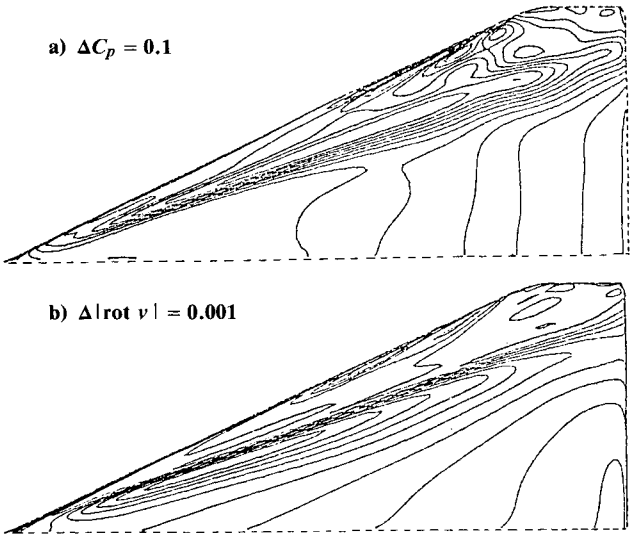

Fig. 9 Leeward surface contour lines of constant C_p and $|\text{rot } v|$ for $M_\infty = 0.85$, $\alpha = 10°$, $Re_{\infty,c_R} = 2.38 \times 10^6$.

the primary separation line. Where the skin friction lines diverge, a dashed line suggests the attachment line of, presumably, the secondary vortex. The pattern of diverging streamlines ceases just ahead of the cropped tip, and apparently the secondary attachment line terminates there. We believe this effect is strongly influenced by the shape of the tip.

The secondary separation line almost coincides with the pressure minimum (Fig. 9a). Large gradients of the modulus of vorticity (Fig. 9b) can be seen where the boundary layer lifts off the surface. Pressure and vorticity are nearly conical up to $x/c_R \sim 0.55$. The structure in the flow near the leading edge between $x/c_R \sim 0.55$ and ~ 0.75 is complex and needs to be discussed further. For this purpose, Fig. 10 presents contour curves of constant static C_p, total pressure coefficient $C_{p_t} = 1 - p_t/p_{t_\infty}$, and vorticity modulus drawn in the true plane $x/c_R = 0.80$. The rings of static C_p (Fig. 10a) identify the primary vortex. The overall pattern of these contours is regular except for the region between the primary vortex and the leading edge. The contours of total pressure (Fig. 10b) and vorticity modulus (Fig. 10c) show the thinness of the boundary layer on the upper and lower surfaces. They also indicate the lifting up of the boundary layer on the upper surface just under the primary vortex. This is confirmation that secondary separation occurs under the primary vortex where the contour lines of C_{p_t} and vorticity on the upper surface are most dense. Further outboard, both sets of contours show another uplifting from the wing surface and could be called a tertiary separation. Even a fourth island of vorticity appears very near the leading edge.

The comparison of static pressure coefficients (Fig. 11) at the stations $x/c_R = 0.3$, 0.6, and 0.8 with experimental data verifies the realism of the main features simulated here and points out the contrast with the Euler solution. The position of

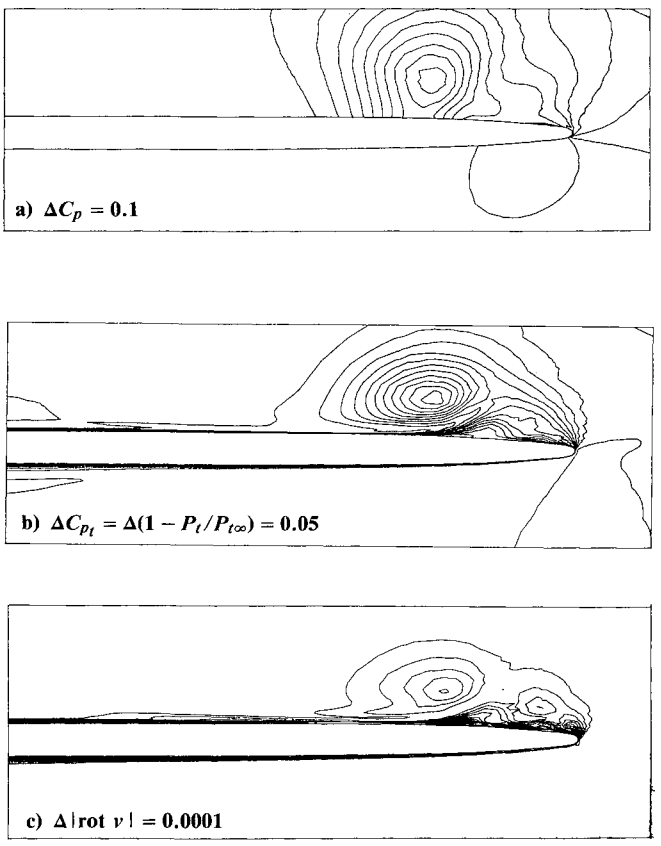

Fig. 10 Contour lines in the plane $x/c_R = 0.80$.

the primary vortex core and the pressure level under it are predicted in good agreement with the experiment, whereas the pressure minimum in the Euler solution lies too close to the leading edge and its suction is much higher. A number of different C_p measurements were taken for different Reynolds numbers. The results of these measurements show a clear dependence on the Reynolds number. Since our simulation is for laminar flow, we compare here with the measurements[11] taken at the lowest Reynolds number because that case contains the largest region of laminar flow. Two distinct minima occur in the viscous simulation, which is typical of laminar vortex flow. The second minimum usually is not seen in turbulent flow, and this is consistent with the experimental results presented here, in which the transition to turbulence was observed. The comparison of laminar and turbulent pressure measurements over a delta wing (Fig. 12) illustrates this effect, which Küchemann discusses in his book.[10] The third minimum in the computed pressure near the leading edge at $x/c_R = 0.6$ (Fig. 11) may be related to the third vortical structure seen near the leading edge in Fig. 10c.

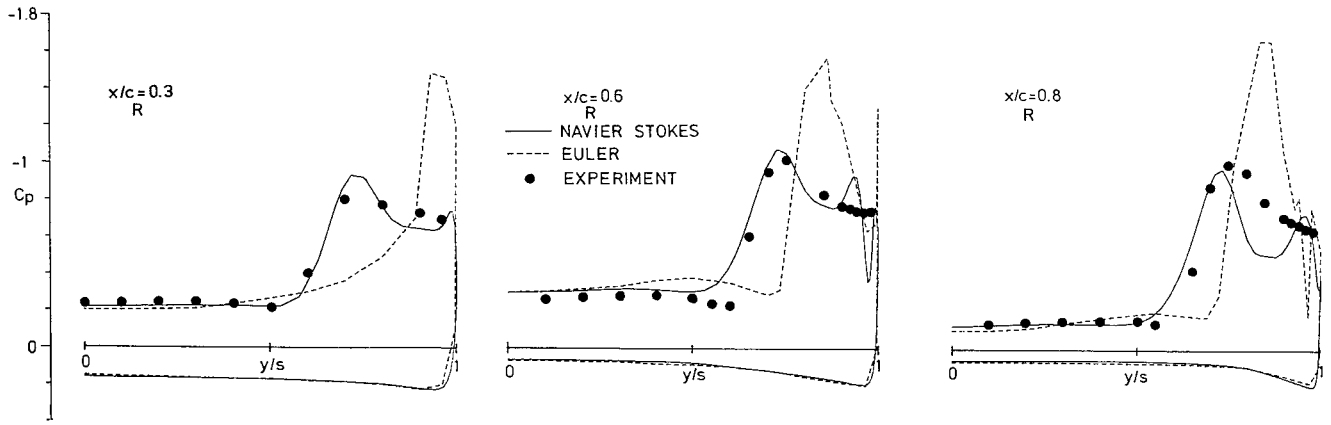

Fig. 11 Comparison of measured surface pressure coefficient with those computed by Euler and Navier-Stokes equations: $M_\infty = 0.85$, $\alpha = 10$ deg, $Re_\infty = 2.38 \times 10^6$.

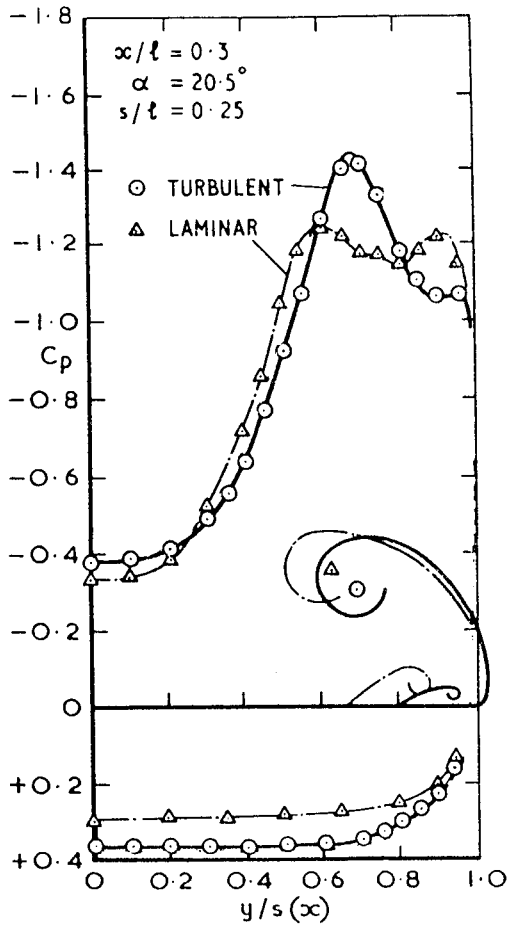

Fig. 12 Differences in measured surface pressures on a delta wing in laminar and in turbulent flow.[10]

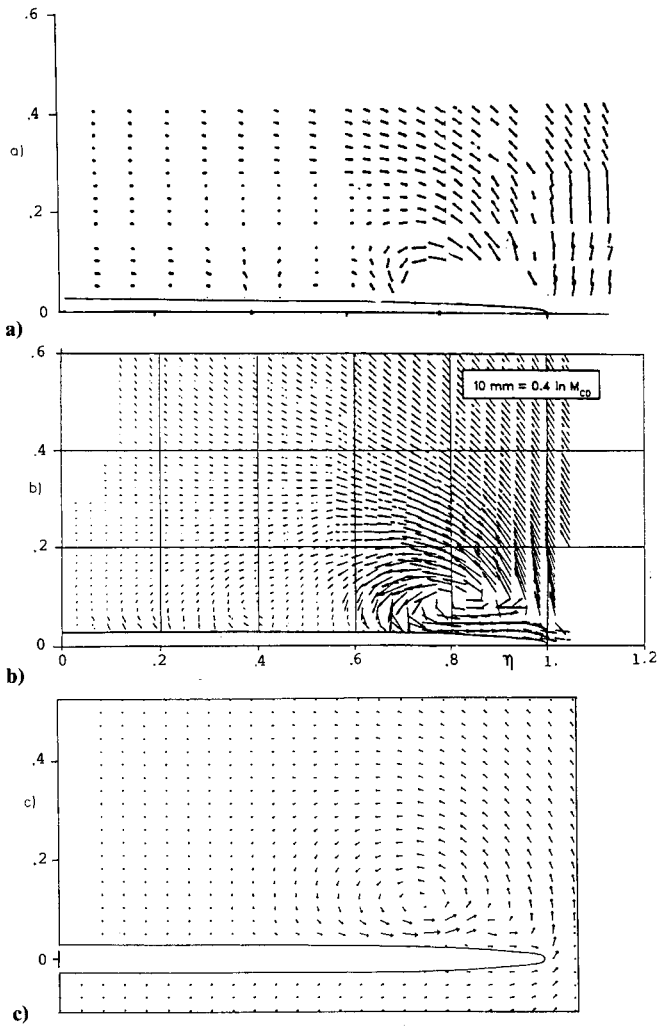

Fig. 13 Comparison of velocity vectors over the wing at $x/c_R = 0.8$ from a) laser measurements, b) seven-hole probe measurements, and c) the Navier-Stokes solution.

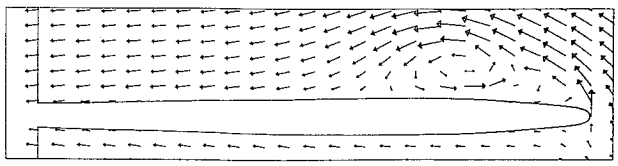

a) Overall view

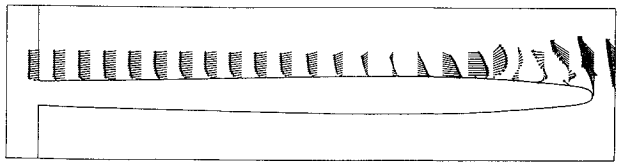

b) Boundary-layer profile

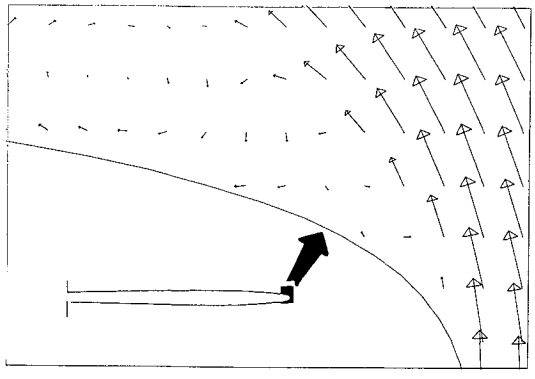

c) Detail showing fourth clockwise vortex at leading edge

Fig. 14 Velocity vectors drawn in the plane normal to the leading edge at $x/c_R = 0.70$.

The overall comparison of the velocity vectors in Fig. 13 measured by two different techniques (laser[14] and probe[12]) and those from the computed solution further support the realism of the calculation. We should point out that even under the best of circumstances such measurements are difficult to carry out for transonic flow. As seen in Fig. 13a, laser measurements could not resolve the entire primary vortex core, and the probe measurements just outboard of the leading edge in Fig. 13b are clearly in error. Nevertheless, these are the best data we have to work with. Close inspection of this figure does show that the core of the primary vortex in the computed solution is slightly above and inboard of the one found in the probe measurements in turbulent flow. The sketch of the primary vortices in Fig. 12, taken from the laminar and turbulent experiments, explains this difference as being due to the turbulent flow condition present during the probe measurements.

We return now to the question of the complex structure seen in the vorticity contours in Fig. 10c. Velocity vectors are needed to bring out the sense of the flow direction. Figure 14 displays them drawn at equispaced intervals (not grid points) in a true plane normal to the leading edge at $x/c_R = 0.70$. (Looking at the vectors in this plane reduces the chances of being mislead because the missing component along the leading edge varies the least.) Here (Fig. 14a) we see clearly the primary separation, the vortex core, and the primary attachment point. The secondary and tertiary vortices are seen only crudely because of the coarse spacing of the vectors. With a tighter spacing over a region close to the upper surface, Fig. 14b brings out the velocity profile over the whole upper surface of the wing section and now clearly indicates the secondary and tertiary vortices. In the region just surrounding the leading edge of the wing the velocity vectors in Fig. 14c even reveal a fourth vortex that might be called a "roller" vortex because it is sandwiched between the shed shear layer and the wing surface. There might be a counterclockwise vortex in the vicinity of the leading edge.

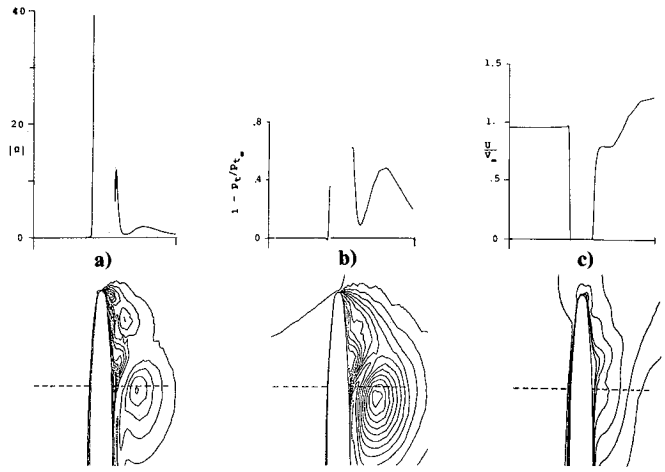

Fig. 15 Profiles through the boundary layer along the dashed line drawn in the plane $x/c_R = 0.8$: a) vorticity modulus, b) total pressure coefficient, c) U/V_∞ velocity component.

In high Reynolds number flows one expects the boundary layer to be very thin. In order to investigate this matter in our solution, we present diagram plots of vorticity, total pressure, and u component of velocity drawn versus the line segment indicated by the dashed line in the contour plots in Fig. 15. These diagrams indicate the very thin and sharp boundary layer profile supported by our mesh clustered tightly near the wing surface. It is interesting to observe that the maximum of vorticity (Fig. 15a) occurs in the boundary layer on the windward side, presumably because the boundary layer is swept and stretched there. The magnitude of vorticity is much higher in both the windward and leeward side boundary layers than in the core of the primary vortex. This suggests that the standard Baldwin and Lomax model for turbulence could be applied in its usual form without modifying its use of vorticity provided that the first maximum $F(z) = z\,|\text{rot } v|\,[1-\exp(-z^+/26)]$ is chosen to define $F_{\max}$ and $z_{\max}$. The largest loss in total pressure occurs in the leeward boundary layer (Fig. 15b), but here the loss in the core is greater than in the windward boundary layer. The profiles of the u velocity component show that the gradient of u is somewhat steeper through the windward boundary layer than it is through the leeward layer where it is separating. The small plateau in u is a curious feature of this uplifting layer.

Concluding Remarks

The quantitative details of this solution must be analyzed further before one can come to a final judgment about its realism. But from comparison with experimental data we can conclude that the laminar Navier-Stokes equations are a better model than the Euler equations for this class of flow, and that in overall qualitative terms their numerical solution is predicting the interaction between the primary and secondary vortices, and thus the surface pressure, more accurately than the inviscid flow simulation. It remains to be investigated what improvements can be gained by implementing simple transition and turbulence models for high Reynolds number vortical flows.

Acknowledgments

The authors thank Dr. G. Drougge, Aeronautical Research Institute of Sweden (FFA), for valuable discussions. The development of the Navier-Stokes code was supported in part by the Swedish Board for Technical Development (STU) and by an Office of Naval Research grant during the first author's sabbatical visit at M.I.T. The actual computations were carried out with the support of the Institute of Mathematics and its Applications (IMA) of the University of Minnesota, with funds provided by the National Science Foundation (NSF).

References

[1]Smith, J. H. B., "Vortex Flows in Aerodynamics," *Annual Review of Fluid Mechanics,* Vol. 18, edited by M. Van Dyke, Annual Reviews, Palo Alto, CA, 1986, pp. 221–242.

[2]Newsome, R. W. and Kandil, O. A., "Vortical Flow Aerodynamics—Physical Aspects and Numerical Simulation," AIAA Paper 87-0205, Jan. 1987.

[3]Rizzi, A. and Purcell, C. J., "On the Computation of Transonic Leading-Edge Vortices Using the Euler Equations," *Journal of Fluid Mechanics,* Vol. 181, April 1987, pp. 163–195.

[4]Elsenaar, A. and Eriksson, G. (eds.), *Proceedings of the International Vortex Flow Experiment on Euler Code Validation,* Aeronautical Research Institute of Sweden, Stockholm, FFA TN, 1986.

[5]Müller, B. and Rizzi, A., "Navier-Stokes Computation of Transonic Vortices Over a Round Leading Edge Delta Wing," AIAA Paper 87-1227, June 1987.

[6]Rizzi, A. and Eriksson, L.-E., "Computation of Flow Around Wings Based on the Euler Equations," *Journal of Fluid Mechanics,* Vol. 148, Oct. 1984, pp. 45–71.

[7]Eriksson, L.-E., "Generation of Boundary Conforming Grids Around Wing-Body Configurations Using Transfinite Interpolation," *AIAA Journal,* Vol. 20, Oct 1982, pp. 1313–1320.

[8]Rizzi, A., "Vector Coding the Finite-Volume Procedure for the CYBER 205," *Parallel Computing,* Vol. 2, No. 1, 1985, pp. 295–312.

[9]Bannink, W. J. and Houtman, E. M., "Experiments on the Transonic Flow over a Delta Wing at High Angles of Attack," *Proceedings of the International Vortex Flow Experiment on Euler Code Validation,* Aeronautical Research Institute of Sweden, Stockholm, FFA TN, 1986, pp. 37–46.

[10]Küchemann, D., "The Aerodynamic Design of Aircraft," Pergamon, Oxford, England, 1978, pp. 390–391.

[11]Hartmann, K., "Force and Pressure Measurements Including Surface Flow Visualizations on a Cropped Delta Wing," *Proceedings of the International Vortex Flow Experiment on Euler Code Validation,* Aeronautical Research Institute of Sweden, Stockholm, FFA TN, 1986, pp. 63–88.

[12]Hjelmberg, L., "Test on a 55° and 65° Delta Wing at FFA," *Proceedings of the International Vortex Flow Experiment on Euler Code Validation,* Aeronautical Research Institute of Sweden, Stockholm, FFA TN, 1986, pp. 89–106.

[13]Rizzi, A., Drougge, G., and Purcell, C. J., "Euler Simulation of Shed Vortex Flows over the 65 Degree Delta Wings," *Proceedings of the International Vortex Flow Experiment on Euler Code Validation,* Aeronautical Research Institute of Sweden, Stockholm, FFA TN, 1986, pp. 289–344.

[14]Bütefisch, K. A., Pallek, D., and Reichmuth, J., "Flow-Field Study on a 65° Delta Wing," *Proceedings of the International Vortex Flow Experiment on Euler Code Validation,* Aeronautical Research Institute of Sweden, Stockholm, FFA TN, 1986, pp. 107–115.